Trends in Physical Chemistry
Vol. 20, 2020

Mini-Review

Photophysical properties of zirconium-oxide metal organic frameworks containing transition metal polyimine guests: A mini-review

Jacob M. Mayers and Randy W. Larsen

Department of Chemistry, University of South Florida, 4202 East Fowler Ave., Tampa, FL 33620, USA.

ABSTRACT

The drive towards sustainable energy has led to the development of metal organic frameworks (MOFs) containing photoactive elements, either as guests or as elements of the framework itself. A large number of highly stable Zr-O-based MOFs that contain either transition metal polyimine guests or free-base and metalloporphyrin ligands have now been reported with unique photophysical properties. Here, a review of Zr-O MOFs containing Ru(II) polyimines is presented with an emphasis on the relationship between the photoactive element photophysics and MOF structure. An understanding of such relationships is essential for the future design of materials with applications in light harvesting and solar photochemistry.

KEYWORDS: metal organic frameworks, ruthenium polyimines, photophysics, MLCT states, Uio-66, Uio-67.

INTRODUCTION

Light responsive materials are important components of a wide range of technologies including sustainable energy systems, human health, environmental remediation and greenhouse gas mitigation. Photoactive materials consist of chromophores either encapsulated within pores or cavities associated with the material or as a component of the material itself. To date, light-sensitive materials have been developed based upon photoactive polymers, hydrogels, glasses and inorganic composites [1-5]. Of particular interest are porous materials that can accommodate light-sensitive guest molecules or substrates for photocatalysis. One class of porous materials that has emerged for light-harvesting applications are the metal organic framework materials (MOFs). The development of MOF-based photoactive materials exploits the high porosity, geometrically diverse metal building blocks (MBBs) and variable geometry/length organic linkers to produce materials containing either encapsulated photoactive guests or photoactive linkers that are a component of the framework itself. The general paradigm for MOF assembly involves the coupling of metal building blocks (MBBs) with organic linkers to form regularly porous three-dimensional structures with pre-selected topologies. The topology is based upon the geometry of the MBB and the orientation of the functional groups associated with the connecting ligand. With regard to light harvesting applications, the regular porosity of MOF topologies provides ample opportunities to encapsulate photoactive guests (Fig. 1).

One class of MOFs which is particularly important for photocatalytic applications are those containing zirconium (IV) oxide clusters as the MBB [2]. Zirconium (IV) oxide clusters are easily formed in arrangements $(ZrO_2)_n$ and exhibit high thermal and water stability. Connection between $(ZrO_2)_n$ clusters and either organic carboxylate or amine linkers has led to the development of a large series of MOFs which exhibit exceptional gas sorption, gas separation, catalytic, and drug delivery properties relative to other transition metal-based MOFs [3-7]. High valent transition metal cations such as Cr(IV)

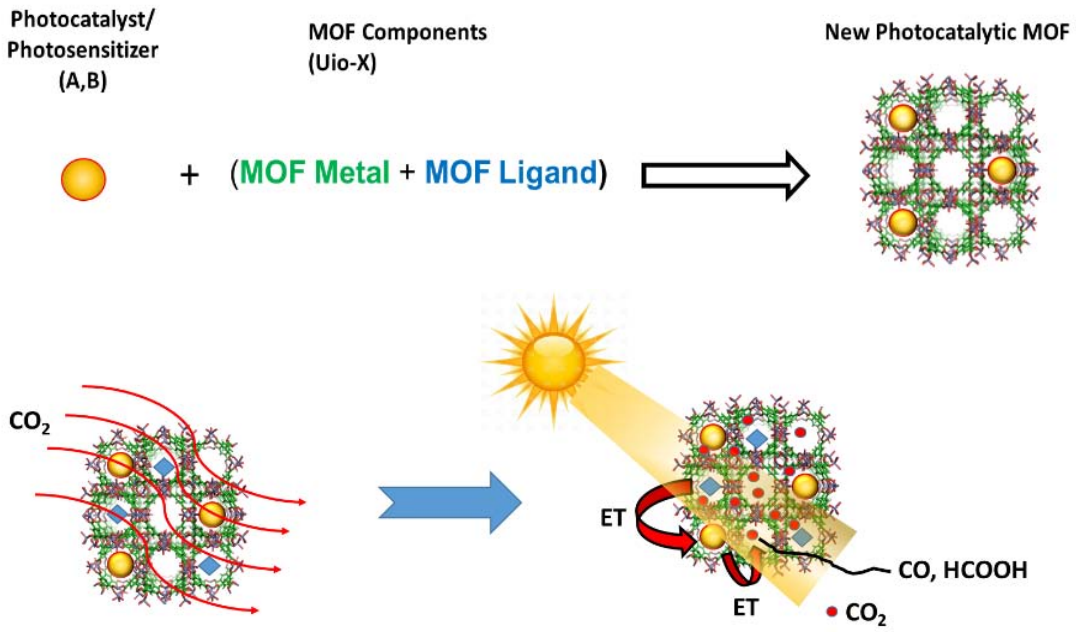

Fig. 1. Diagram illustrating the assembly (top) and photocatalysis (bottom) of light harvesting MOFs containing photoactive guest molecules.

and Ti(IV) also produce stable MOF structures and these materials have also shown versatile applications. The geometry of organic linkers along with the Zr-O empirical arrangement allows for a variety of MOF topologies including NU-1000, Uio-66, and PCN-1000, being the most common (Fig. 2) [8-10].

The hydrothermal stability of Zr-based MOFs arises from a number of factors including the oxidation state of the metal ion, the charge and geometry of the connecting ligand, and core hydrophobicity [11]. The high oxidation state of the Zr (IV) core increases the metal-ligand bond strength resulting in significant thermal and solvent stability of the MOFs [12]. Modulation of the ligand hydrophobicity can further enhance the water stability of the zirconium framework by increasing the non-polar nature of MOF pores. The topology of ZrO-based MOFs is highly dependent upon the organic ligand used in the solvothermal synthesis of the framework. The Zr oxide clusters can form in a number of empirical arrangements which includes the most common hexanuclear arrangement $Zr_6(\mu_3\text{-}O)_4(\mu_3\text{-}OH)_4$ or Zr_6O_8. Other arrangements such as Zr_8O_6, ZrO_7, ZrO_8, and ZrO_6 are possible but less common relative to the hexanuclear clusters. The octahedral Zr_6O_8 cluster is associated with carboxylate ligands that range from twelve carbon connections ($Zr_6(\mu_3\text{-}O)_4(\mu_3\text{-}OH)_4(\text{-}CO_2)_{12}$ to eight ($Zr_6(\mu_3\text{-}O)_4(\mu_3\text{-}OH)_4(\text{-}CO_2)_8$ and six ($Zr_6(\mu_3\text{-}O)_4(\mu_3\text{-}OH)_4(\text{-}CO_2)_6$. The use of benzene dicarboxylic acid (BDC) with $ZrCl_4$ produces 12 carbon connected Zr-O clusters $Zr_6(\mu_3\text{-}O)_4(\mu_3\text{-}OH)_4(\text{-}CO)_{12}$ with *fcu* topology and are referred to as Uio-66 (University of Oslo) [13]. Extension of the BDC linker (biphenyl dicarboxylic acid and triphenyl dicarboxylic acid) results in a MOF with similar *fcu* topology and higher surface areas, and are referred to as Uio-67 and Uio-68, respectively. The use of a 4-carbon connected linker (tetracarboxyphenylporphyrin) along with the cuboctahedron Zr-clusters generates a different MOF topology (*ftw*) but conserves the identity of the Zr cluster arrangement ($Zr_6(\mu_3\text{-}O)_4(\mu_3\text{-}OH)_4\,(\text{-}CO)_{12}$) (MOF-525) [14]. Distinctive MOF topologies also possess pores with wide ranging dimensions. For example, Uio-66 contains both a 8 Å tetrahedral and 12 Å octahedral cage while MOF-808, constructed using BTCA and containing trigonal antiprism Zr clusters $Zr_6O_4(OH)_4(BTC)_2(HCOO)_6$ with overall *spn* topology, possesses tetrahedral cages of ~5 Å along with repeating adamantane cages of ~18 Å [15, 16].

The availability of cavities with varying dimensions in Zr-O-based MOFs affords enormous opportunities

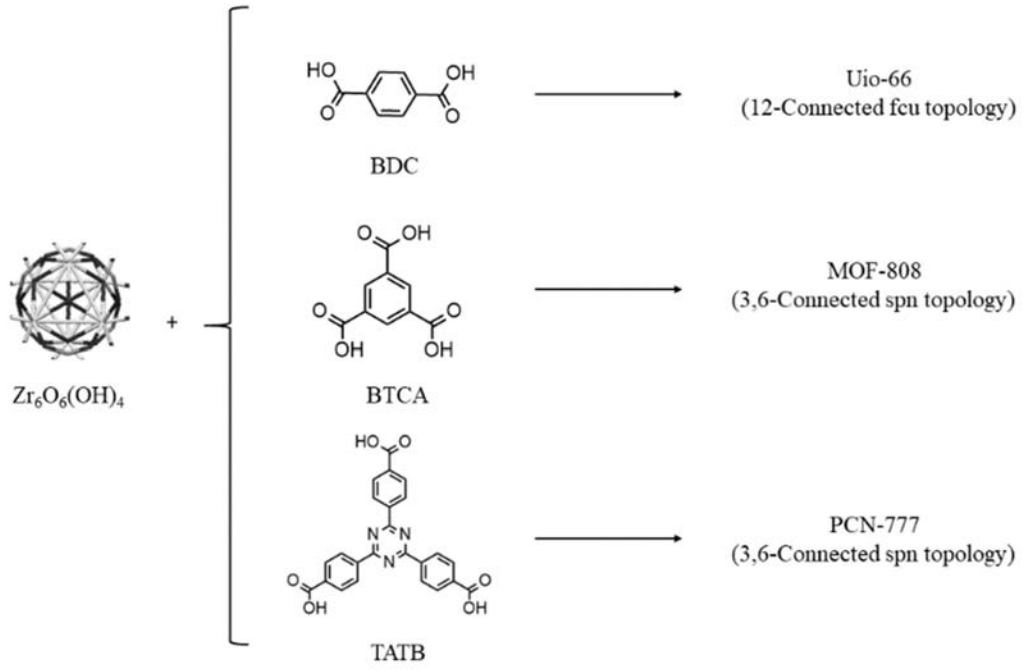

Fig. 2. Illustartion of the ligands used to form the three most common ZrO-based MOFs.

to encapsulate photoactive guest molecules for applications in light harvesting. The additional robustness of the crystalline material enables applications in a wide range of environments from industrial photo reactors to environmentally deployed solar photochemistry systems. The range of guests includes free base and metallo porphyrins, transition metal polyimines, polyoxometalates (POMs), and various organic molecules with extended π-systems.

Ruthenium polyimines

A particularly important class of photoactive guests are the transition metal polyimines, most notably $[Ru(II)(2,2'\text{-bipyridine})_3]^{2+}$ (RuBpy) and its derivatives. The RuBpy complex exhibits prominent absorption in the visible region (λ_{abs} = 450 nm) with a relatively high molar absorptivity (ε_{450} = 14,500 M^{-1} cm^{-1}). Visible light absorption is primarily due to electron displacement from the Ru (II) ion (t_{2g} molecular orbital) to a π* molecular orbital on one of the bipyridine ligands (metal to ligand charge transfer, MLCT). The initial ^{1}MLCT excited state decays within femtoseconds to a manifold of three closely spaced ^{3}MLCT states (Fig. 3). Decay of the ^{3}MLCT state manifold occurs through multiple pathways: (1) radiative decay to the ground state associated with competitive radiative (k_r) and non-radiative transitions (k_{nr}) and (2) thermal population of a ligand field state (^{3}LF) which is anti-bonding with respect to the Ru-N bond and is

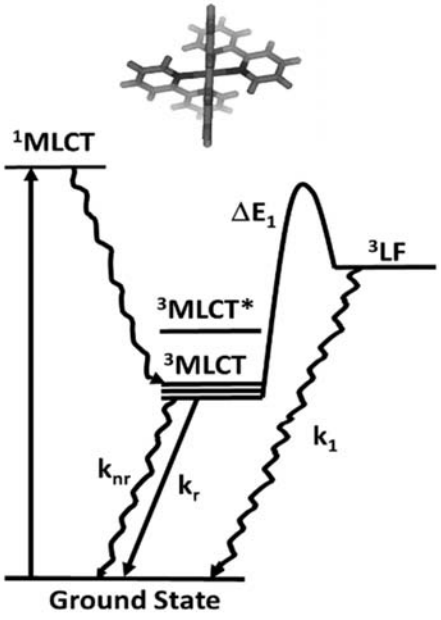

Fig. 3. Diagram of the excited state decay pathways for RuBpy.

accompanied by an expansion of the complex [17]. The decay pathways are highly dependent upon the molecular environment including temperature and solvent.

RuBpy as a non-covalent guest in Zr-O-based MOFs

The physical dimensions (~ 12 Å diameter) and overall thermal and photo stability of RuBpy makes this cation an attractive candidate for encapsulation within Zr-O-based MOFs (Fig. 4). Two strategies have been employed thus far to encapsulate RuBpy-type complexes within the Uio-series of MOFs. The first strategy utilizes a 'one pot' method for non-covalent encapsulation [18, 19]. Both RuBpy and [Ru(II)tris(1,10-phenanthroline)]$^{2+}$ (RuPhen) have been non-covalently encapsulated within the octahedral cavities of Uio-66 and Uio-66-NH_2. Previous studies have demonstrated that non-covalent encapsulation of RuBpy or RuPhen into zinc-based polyhedral networks results in changes in the steady-state emission energy and ^{3}MLCT emission lifetimes [20-22]. For many Zn-carboxylate-based and Cd-carboxylate MOFs, the RuBpy cation serves as a templating agent forming materials with crystallographically resolvable RuBpy complexes within the frameworks and unique photophysical properties (RWLC series of MOFs) [23-26].

One of the first examples of non-covalent encapsulation of a Ru(II) polyimine within a Zr-O MOF involved the synthesis of RuBpy@Uio-66. For the RuBpy@Uio-66 MOF the RuBpy did not serve as a templating agent as the parent Uio-66 structure is retained regardless of the presence of RuBpy cations. The materials were synthesized using a 'one-pot' solvothermal strategy in which $ZrCl_4$, benzene 1,4-dicarboxylate and RuBpy were heated in N,N'-dimethylformamide containing a small amount of glacial acetic acid. The resulting orange material was found to have the same X-ray powder diffraction pattern as the parent Uio-66. Although single crystal X-ray structures have not been reported for this material it is likely that the RuBpy occupies the 12 Å octahedral cage with a loading of ~ 0.3 μmoles of RuBpy per mg of RuBpy@Uio-66.

Encapsulation of RuBpy into Uio-66 results in a bathochromatic shift of the steady-state emission

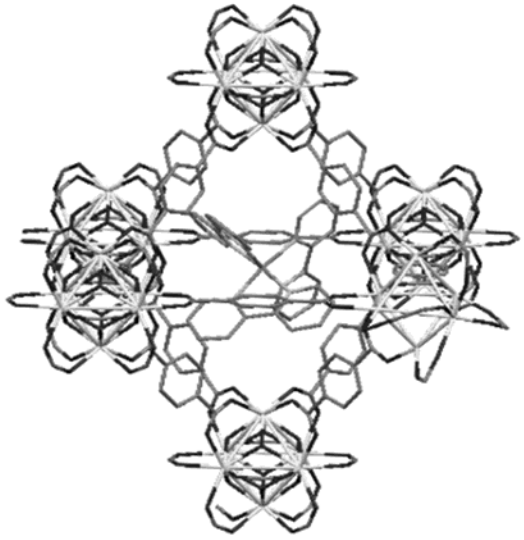

Fig. 4. Model illustrating RuBpy encapsulated within the large cavity of Uio-66.

band relative to RuBpy in solution due to a decrease in the E_{00} of the emitting ^{3}MLCT state resulting from stabilization of the excited state dipole of RuBpy by the hydroxyl groups of the zirconium oxide clusters ($Zr_6O_4(OH)_4$) (Fig. 5). Analysis of the emission data using a Franck-Condon approach also demonstrates that the average high frequency accepting modes ($h\omega_H$) are similar to RuBpy in ethanol which consist of totally symmetric (A_1) inter-bipyridine C-C stretching, C-N stretching, and CCH bending modes [27]. The low frequency acceptor modes ($h\omega_L$) are similar between RuBpy@Uio-66 and RuBpy in solution which consist mainly of Ru-N stretching. Although the high and low average vibrational acceptor mode frequencies are similar between RuBpy in solution and RuBpy@Uio-66, the Huang-Rhys factors pertaining the low frequency modes, S_L, decrease for RuBpy@Uio-66 relative to solution values. (Table 1) As this factor is related to the coupling between the excited state and ground state facilitated by low frequency vibrations, changes in this value reflects possible distortions of the complex upon encapsulation that shifts the excited state potential surface along the coordinate axis. In the case of RuBpy@Uio-66 the extent of these displacements can be determined using:

$$S_i = M(1/2)(h\omega_i/\hbar)(\Delta Q)^2 \qquad \text{Eq. 1}$$

where M is the reduced mass of the vibration system. The geometry term is proportional to the

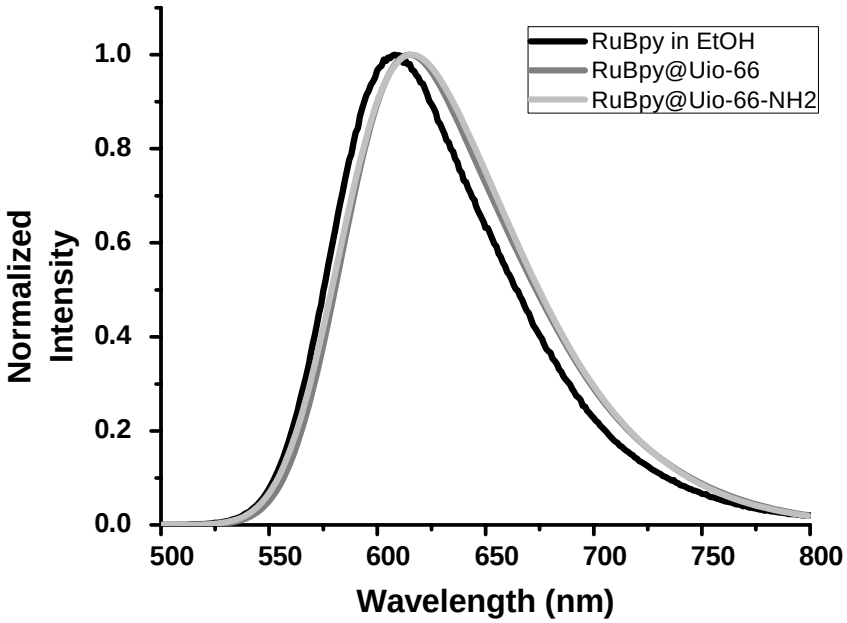

Fig. 5. Steady emission spectra of RuBpy in ethanol, RuBpy@Uio-66 and RuBpy@Uio-66-NH2.

Table 1. Steady-state emission data for RuBpy in solution, RuBpy@Uio-66, RuBpy@Uio-66-NH_2, RuPhen in solution, RuPhen@Uio-66, and RuPhen@Uio-66-NH_2 at 25 °C. The values of E_{00}, hω, and $\nu_{1/2}$ are all in cm^{-1}. The λ_{em} values are in nm.

Sample	λ_{em}	E_{00}	$h\omega_H$	$h\omega_L$	S_H	S_L	$\nu_{1/2}$
*RuBpy	608	16908	1265	237	0.64	0.95	1604
RuBpy@Uio-66	615	16651	1387	304	0.63	0.71	1640
*RuBpy@Uio-66-NH_2	615	16597	1172	228	0.7	0.84	1762
*RuPhen	588	17405	1273	247	0.6	0.96	1581
*RuPhen@Uio-66	599	16983	1259	270	0.63	0.77	1711
*RuPhen@Uio-66-NH_2	602	16909	1240	276	0.62	0.76	1643

*Samples were prepared as a suspension in ethanol. All other samples were prepared as solids.

Huang-Rhys term and inversely proportional to the average coupling modes. By rearranging Eq. 1 a ratio of the ground-state:excited state potential surface displacements can be obtained:

$$(\Delta Q_{MOF})/\Delta Q_{Sol}) = (S^{MOF}h\omega_{sol}/ S^{Sol}h\omega_{MOF})^{1/2} \quad \text{Eq. 2.}$$

The average ratio (using both high and low frequency coupling mode parameters) is ~ 0.86 for RuBpy@ Uio-66 indicating a better overall coupling between the emitting ^{3}MLCT and the ground state (Fig. 6).

The corresponding emission lifetime of encapsulated RuBpy exhibits biphasic decay kinetics indicating two populations in RuBpy@Uio-66 (Fig. 7). One of the populations exhibits a lifetime greatly extended relative to RuBpy in solution (τ_1 ~ 1000 ns vs. τ_{sol} ~ 630 ns) which is consistent with reduced access to the ^{3}LF state from the ^{3}MLCT manifold (Fig. 3). As the ^{3}LF state is composed of molecular orbitals that are anti-bonding with respect to Ru – N bond, confinement that restricts the physical expansion of the RuBpy complex raises the energy barrier required to access the ^{3}LF state. The excited decay parameters can be obtained by fitting the lifetime decay of RuBpy as a function of temperature to:

$$(1/\tau_{obs}) = k_0 + k_1*\exp(-\Delta E_1/k_bT) \quad \text{Eq. 3}$$

where k_0 is the sum of the radiative and non-radiative rate constants for decay through the lowest energy ^{3}MLCT manifold ($k_0 = k_r + k_{nr}$), and both k_1 and ΔE_1 are as described in Fig. 3, k_b is Boltzmann's constant and T is the temperature. The data for RuBpy and RuBpy@Uio-66 are summarized in (Table 2). Interestingly, the ΔE_1 value actually decreases for the population giving rise to the slower decay phase which would be consistent with a much faster decay than what is observed in solution. Alternatively, the data are consistent with the ΔE_1 being sufficiently high such that the ^{3}LF state has become completely inaccessible and the observed barrier is that needed to access another ^{3}MLCT state closer in energy to the lowest energy ^{3}MLCT manifold. The magnitude of the k_1 value further indicates that this state may be more singlet-like in character. The fact that the k_0 value is relatively unaltered suggests that encapsulation does not affect the decay pathways from the emitting ^{3}MLCT state (Fig. 8) [27, 28].

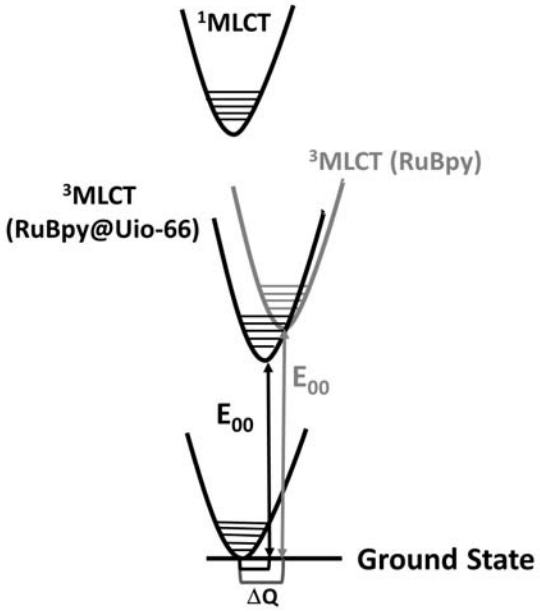

Fig. 6. Diagram illustrating the difference in RuBpy ^{3}MLCT states between RuBpy in solution and RuBpy@Uio-66.

The second population of RuBpy encapsulated within Uio-66 exhibits a lifetime that is significantly reduced relative to RuBpy in solution (τ_2 ~ 190 ns). Examination of the data in (Table 2) reveals that this population of RuBpy is in an environment which partially confines the complex resulting in an increase in ΔE_1 ($\Delta\Delta E_1$ ~ 800 cm^{-1}) with a non-radiative decay rate that is nearly 50-fold higher than for RuBpy in solution. This is consistent with enhanced vibronic coupling between the ^{3}LF state

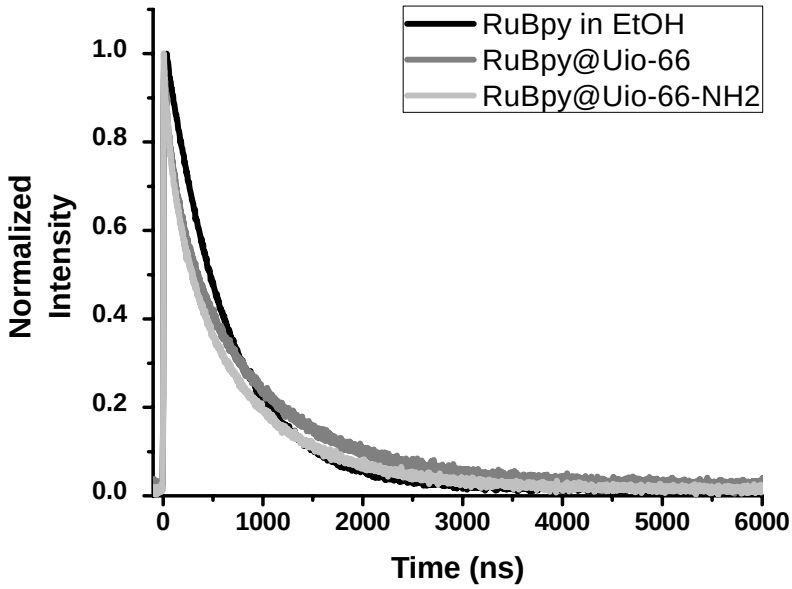

Fig. 7. Emission decays for RuBpy, RuBpy@Uio-66 and RuBpy@Uio-66-NH2 at 25 ^{o}C.

Table 2. Kinetic parameters for RuBpy in solution, RuBpy@Uio-66 and RuBpy@Uio-66-NH_2 obtained from fits of the lifetime decays to Eq. 3.

Sample	k_0 x10^5 (s^{-1})	k_1 x10^{13} (s^{-1})	ΔE_1 (cm^{-1})	Lifetime (ns)
RuBpy	6	2	3491	620
RuBpy@Uio-66				
Fast Phase	66	103	4292	187
Slow Phase	9	0.05	2986	1004
RuBpy@Uio-66-NH_2				
Fast Phase	113	796	4671	122
Slow Phase	11	0.2	3079	894

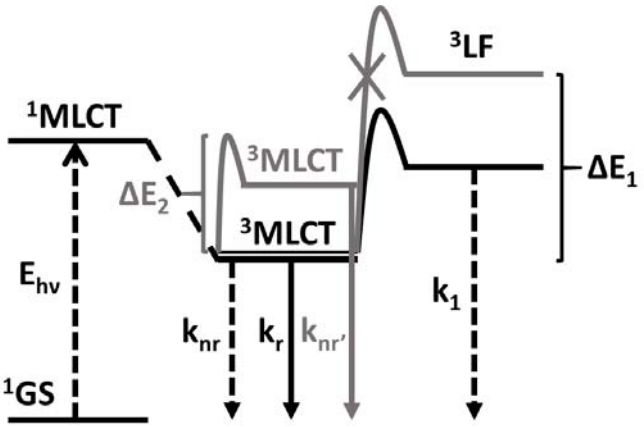

Fig. 8. Diagram illustrating the difference in RuBpy ^{3}MLCT states between RuBpy in solution and RuBpy@Uio-66.

and the singlet ground state. In addition, the k_0 value for this population is also increased by an order of magnitude indicating enhanced deactivation of the lowest energy ^{3}MLCT state. An increase in the k_0 term can be attributed to a quenching of the ^{3}MLCT state where $k_0 = k_r + k_{nr} + k_q$ (k_q = quenching rate constant). The quenching of RuBpy could be due to the presence of a co-encapsulated exogenous quencher formed during the synthesis of RuBpy@Uio-66 or possibly other interactions between the RuBpy and framework that enhance non-radiative decay pathways.

The $[Ru(II)(1,10\text{-phenanthroline})_3]^{2+}$ (RuPhen) complex has also been encapsulated non-covalently within Uio-66 [19]. The RuPhen complex exhibits similar photophysical properties as RuBpy but has a larger excited state dipole moment (6.7D vs 4.6D for RuBpy) which allows for a better understanding of excited state stabilization associated with the Uio-66 cavities [29-31]. As with RuBpy@Uio-66, the emission spectrum of RuPhen@Uio-66 is bathochromically shifted by 11 nm relative to RuPhen in ethanol consistent with the lower E_{00} value supporting stabilization of the excited state dipole moment by the zirconium oxide clusters (Fig. 9). The RuPhen complex exhibits similar average high and low frequency acceptor modes as RuBpy that consist primarily of phenyl ring C-C stretching (high ~ 1273 cm^{-1}) and Ru-N (low ~ 247 cm^{-1}) similar to those observed for RuPhen in solution. The Huang-Rhys factor between RuPhen in solution and RuPhen@Uio-66 are also similar to RuBpy@Uio-66 with the low frequency Huang-Rhys factor (S_L) being slightly lower than that observed for RuPhen in solution (Table 1). The average ratio of the potential surface displacement between the ground state and

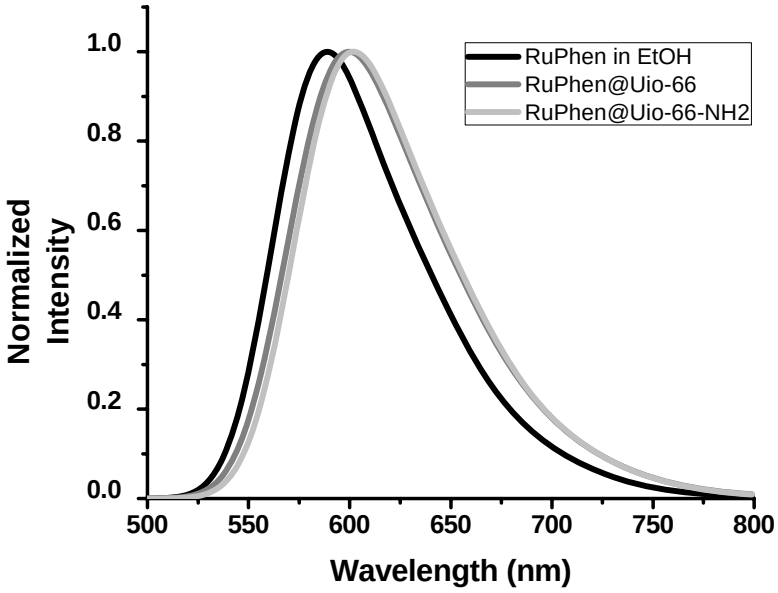

Fig. 9. Steady emission spectra of RuPhen in ethanol, RuPhen@Uio-66 and RuPhen@Uio-66-NH2.

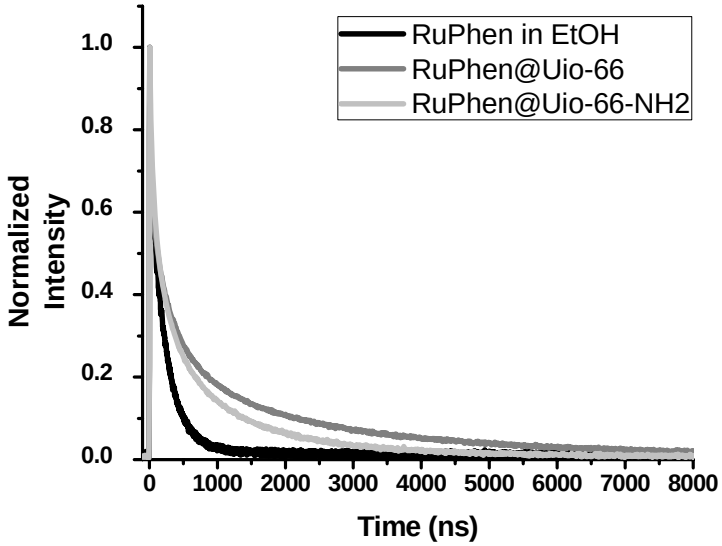

Fig. 10. Emission liefime data for RuPhen in ethanol, RuPehn@Uio-66 and RuPhen@Uio-66-NH2 at 25 ^{o}C.

^{3}MLCT of RuPhen relative to RuPhen@Uio-66 (using both high and low frequency coupling mode parameters) is ~ 0.95 indicating very little perturbations upon non-covalent encapsulation. Overall, the effect of the increased excited state dipole moment is to further reduce the E_{00} value associated with the ^{3}MLCT energy (ΔE_{00} ~250 cm^{-1} for RuBpy@Uio-66 vs. ~420 cm^{-1} for RuPhen@Uio-66).

As with RuBpy@Uio-66, the emission lifetime of RuPhen@Uio-66 can be fit to a bi-exponential decay process arising from two populations of encapsulated complex (Fig. 10). The population giving rise to the slow phase decay lifetime (τ ~2086 ns) is also likely encapsulated within the octahedral cages of Uio-66 with a ΔE_1 value of 1780 cm^{-1} which is ~1400 cm^{-1} lower than that observed for RuPhen in solution (Table 3). The

Table 3. Kinetic parameters for RuPhen in solution, RuPhen@Uio-66 and RuPhen@Uio-66-NH_2 obtained from fits of the lifetime decays to Eq. 3.

Sample	k_0 x10^5 (s^{-1})	k_1 x10^{11} (s^{-1})	ΔE_1 (cm^{-1})	Lifetime (ns)
RuPhen	2	153	3132	234
RuPhen@Uio-66				
Fast Phase	10	0.8	1780	366
Slow Phase	2	0.1	1843	2086
RuPhen@Uio-66-NH_2				
Fast Phase	12	0.2	1770	263
Slow Phase	2	0.02	1662	1524

decrease in ΔE_1 and 10-fold increase in lifetime relative to solution is consistent with complete deactivation of the ^{3}LF state and access to a higher energy ^{3}MLCT state that is more singlet-in-character. Interestingly, the increased excited state dipole moment appears to have very little effect on the excited state decay channels of the RuPhen within the Uio-66 cavities.

Unlike the RuBpy@Uio-66 MOF, the population of RuPhen giving rise to the fast phase decay ($\tau \sim$ 366 ns) exhibits a ΔE_1 value significantly smaller than that observed for RuPhen in solution, a large decrease in k_1 and an order of magnitude increase in k_0 (Table 3). The k_1 and ΔE_1 values are consistent with the fast phase population also being confined within the Uio-66 octahedral cavities prohibiting access to the ^{3}LF state but allowing access to another singlet-in-character ^{3}MLCT state. The fact that the k_0 value is increased by a factor of 5 indicates a quencher may be co-encapsulated within the octahedral cavities that deactivates the lowest energy ^{3}MLCT state [32-35].

Ru(II) polyimine non-covalent encapsulation within Uio-66-NH_2

An important aspect of light sensitive MOF development using photoactive guest complexes is the ability to tune the photophysics through modification of the frameworks. In the case of the Uio-66 MOF, the cavities can be readily functionalized using BDC ligands containing functional groups at the 2-position of the ring. One such functionalized MOF is Uio-66-NH_2 constructed using a 2-amino BDC linker to produce a structural analog of Uio-66 that exhibits the same overall topology and SBU composition ($Zr_6O_4(OH)_4(CO_2)_{12}$ as Uio-66. The presence of an NH_2 functional group within the MOF cavities provides for potential interactions with the guest including H-bonding sites, excited state electron donor/acceptor groups for photoinduced electron transfer applications and novel 'solvation' sites.

Both RuBpy and RuPhen have now been non-covalently encapsulated within the Uio-66-NH_2 framework (RuBpy@Uio-66-NH_2 and RuPhen@ Uio-66-NH_2) [19]. Examination of the steady state emission spectra for RuBpy@Uio-66-NH_2 and RuPhen@UiO-66-NH_2 reveal very little difference in the emission energy upon introduction of the amine group into the framework cavities and is consistent with ^{3}MLCT stabilization occurring through either solvent reorganization within the MOF or interactions between the RuBpy or RuPhen's excited state dipole moment by the Zr clusters. From the data in Table 1, a decrease in the zero-point energy (E_{00}) is evident for both RuBpy@Uio-66-NH_2 and RuPhen@Uio-66-NH_2 relative to the solution value. Similar to Ru@Uio-66 systems, RuPhen@Uio-66-NH_2 exhibits a greater E_{00} decrease relative to RuBpy@Uio-66-NH_2. The low frequency coupling factors (S_L) for RuBpy@Uio-66-NH_2 and RuPhen@Uio-66-NH_2 are slightly lower than RuBpy or RuPhen in solution while the high frequency coupling factors (S_H) remain unchanged, again similar to RuBpy@Uio-66 and RuPhen@Uio-66.

The emission lifetime of both RuBpy@Uio-66-NH_2 and RuPhen@Uio-66-NH_2 were fit to a biexponential decay function indicating two separate populations within each of the materials (Table 2), similar to RuBpy@Uio-66 and RuPhen@Uio-66. In the case of the RuBpy@Uio-66-NH_2 the slow phase

population exhibited an excited state lifetime of ~890 ns which is longer than RuBpy in solution (620 ns) but shorter than RuBpy@Uio-66 (~ 1 μs). The values of k_0 and ΔE_1 for the slow phase decay are also similar between RuBpy@Uio-66 and RuBpy@Uio-66-NH_2 while the k_1 value is a factor of 4 larger for the RuBpy@Uio-66-NH_2 and is likely responsible for the slightly reduced slow phase lifetime. The corresponding slow phase lifetime of the RuPhen@Uio-66-NH_2 was reported to be ~1.5 μs vs. ~2 μs for the slow phase population of RuPhen@Uio-66 with k_0 and ΔE_1 values being similar between the two materials. The k_1 value for RuPhen@Uio-66-NH_2, on the other hand, is reduced by a factor of ~2, relative to RuPhen@ Uio-66 which also accounts for the reduced slow phase lifetime between the two materials.

The corresponding fast phase component of RuBpy@Uio-66-NH_2 and RuPhen@Uio-66-NH_2 exhibit lifetimes significantly shorter than the corresponding fast phase lifetimes associated with RuBpy@Uio-66 and RuPhen@Uio-66. In the case of the RuBpy@Uio-66 and RuBpy@Uio-66-NH_2 the ΔE_1 values between two MOFs are essentially equivalent and are ~ 1000 cm^{-1} above RuBpy in solution. For RuBpy@Uio-66-NH_2 the values of k_0 and k_1 are both larger than those of RuBpy@ Uio-66 by factors of 2 and 8, respectively. Thus, the NH_2 group has a more pronounced effect on the excited state decay pathways of the fast decay population relative to the slow decay population due to enhanced non-radiative decay constants. Interestingly, for the RuPhen@Uio-66-NH_2 MOF the lifetime of the fast phase population is reduced by nearly 100 ns while the ΔE_1 values only change by ~10 cm^{-1} (lower for the RuPhen@Uio-66-NH_2 MOF). The k_0 values are also nearly identical between the two MOFs and the k_1 value is ~4 times lower for RuPhen@Uio-66-NH_2.

The decrease in RuL_3@Uio-66-NH_2 lifetimes relative (*via* non-radiative decay pathways) to the non-functionalized RuL_3@Uio-66 could arise from either electron or energy transfer between RuL_3 and Uio-66-NH_2 framework. Since the BDC-NH_2 and Zr clusters absorb < 400 nm and the emission of RuL_3 complex is at a significantly lower energy (600 nm), energy transfer processes would not occur. On the other hand, amines tend to be effective quenchers of the Ru(II)L_3 excited states either through an oxidative or reductive quenching mechanism. However, a Rhem-Weller analysis of the free energy (ΔG^0) associated with photoinduced electron transfer between either RuBpy or RuPhen and Uio-66-NH_2 is unfavorable with the free energy for either system being ~+ 9 kcal mol^{-1} [36]. An alternative quenching mechanism may involve non-radiative decay pathways including NH --- π interactions between the MOF framework ligands and the π system of the Bpy or Phen ligands of the Ru(II) complexes. Computational studies have demonstrated an ~ 2 kcal mol^{-1} interaction energy between aromatic NH --- π in model systems [37].

Covalent RuBpy guests in Zr-O frameworks

An alternative encapsulation strategy for RuBpy type complexes and Zr-O type MOFs is through covalent modification of the Zr-O nodes associated with the MOF. The carboxylic acid groups coordinated to the Zr-O nodes can be exchanged with other molecules also containing carboxylate functional groups including carboxylate functionalized RuBpy (Fig. 11). Maza *et al*. [38] utilized this method to prepare Ruthenium (II) bis-(2,2'-bipyridine) (2,2'-bipyridyl-5,5'-dicarboxylic acid) (RuDCBPY) encapsulated Uio-67 in which the Ru complex is covalently attached to the Zr-O node (Fig. 12). The parent Uio-67 MOF consists of $Zr_6(\mu_3\text{-}O)_4(\mu_3\text{-}OH)_4$ clusters connected by biphenyl dicarboxylate linkers (BPDC). The RuDCBPY mimics the BPDC linker allowing for incorporation of the complex into Uio-67. The solvothermal synthesis of Uio-67 in the presence of RuDCBPY results in the complex being incorporated into either the larger octahedral cavities or the smaller tetrahedral cavities since

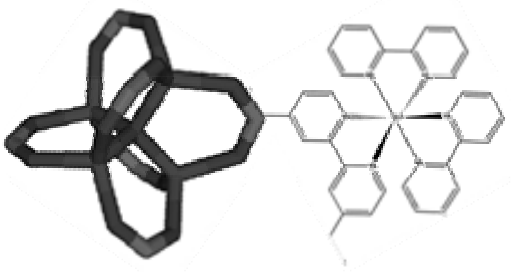

Fig. 11. Diagramatic representation of carboxylate-functionalized RuBpy to the Zr-O node.

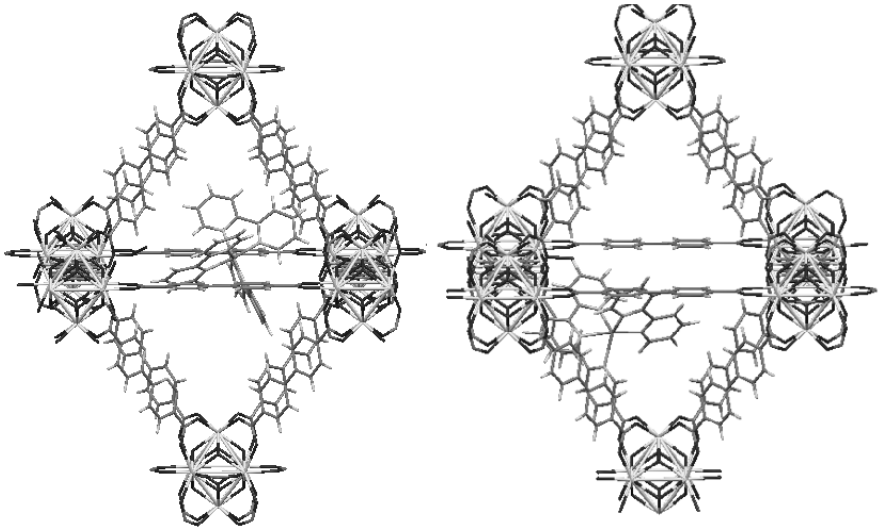

Fig. 12. Encapsulation (left) and incorporation (right) of RuDCBPY in the octahedral cavity of Uio-67.

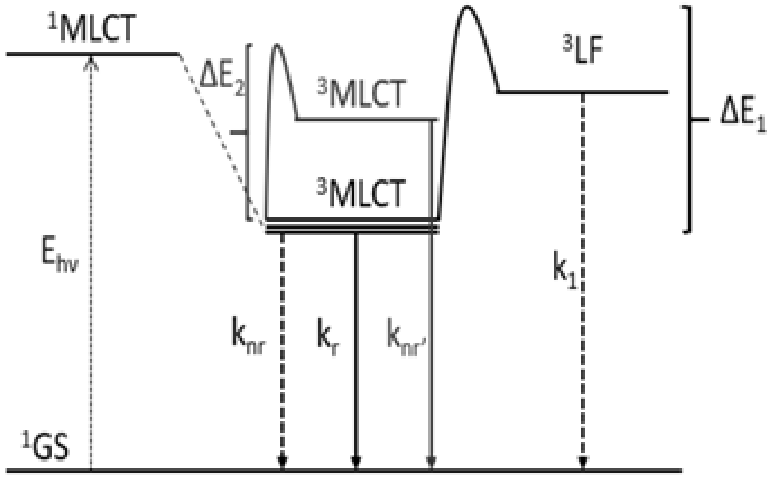

Fig. 13. Energy level diagram of RuDCBPY in solution.

both cavities are large enough to accommodate the complex. In addition to covalent linkages, the RuDCBPY can also be non-covalently encapsulated within the cavities of Uio-67.

In the case of the heteroleptic RuDCBPY complex, the excited MLCT state is localized primarily on the 2,2'-bipyridyl-5,5'-dicarboxylic acid ligand due to the electron withdrawing ability of the carboxylate group that lowers the energy of the π* state relative to 2,2'-bipyridine.The lowering of the DCBPY π* state also results in an increase in the energy barrier required to access the ligand field state (^{3}LF) thereby increasing the observed ΔE_1 (Fig. 13) [33].

The photophysics of RuDCBPY@Uio-67 has been shown to be dependent upon the loading capacity of RuDCBPY. At low RuDCBPY doping concentrations (< 3 mM), the photophysics of RuDCBPY-Uio-67 resemble RuBpy in DMF (Table 4). The emission lifetimes were fit to a single exponential function indicating a single population within RuDCBPY-Uio-67 which is primarily associated with incorporation of RuDCBPY into the backbone of the Uio-67 framework and

Table 4. Summarization of emission lifetimes and extracted kinetic terms at various RuDCBPY doping concentrations.

Sample	Doping Concentration (mM)	k_0 (s^{-1})	k_1 (s^{-1})	ΔE (cm^{-1})	$\tau_{25°C}$ (ns)
RuDCBPY in DMF	----------	$9.6x10^5$	$2.5x10^{11}$	2,500	880
RuBpy in DMF	----------	$8.1x10^5$	$2.2x10^{12}$	3,100	630
RuDCBPY-Uio-67	2.6	$8.2x10^5$	$2.3x10^{11}$	2,700	1,370
RuDCBPY-Uio-67	16.4	$15x10^5$	$1.4x10^{11}$	2,600	645
RuDCBPY-Uio-67 1st phase	20.6	$43x10^5$	$3.0x10^{13}$	2,700	23
RuDCBPY-Uio-67 2nd phase					121
RuDCBPY-Uio-67 1st phase (FTO)	16.6	$8.2x10^6$	--------	--------	21
RuDCBPY-Uio-67 2nd phase (FTO)					208
RuDCBPY-Uio-67 1st phase (FTO)	27.4	$9.9x10^6$	--------	--------	26
RuDCBPY-Uio-67 2nd phase (FTO)					101

positioning of the complex within the larger Uio-67 cavity. Interaction of the DCBPY ligand with the Zr-O cluster likely reduces the electron withdrawing ability allowing for electron delocalization across the complex. Although both the k_0 and k_1 values are similar between RuDCBPY in DMF and RuDCBPY-Uio-67 the difference in decay lifetimes is due to the slight difference in ΔE_1 which has been previously attributed to restricted ability of the complex to expand in the ^{3}LF state.

As the RuDCBPY doping concentrations is increased (7-45 mM) the emission lifetime of RuDCBPY-Uio-67 steadily decreases along with increasing k_0 values. At concentrations above 20 mM the emission decay can be best fit to a biexponential function indicating two distinct populations which is consistent with both covalent incorporation into the framework and non-covalent encapsulation within accessible cavities. The fast decaying population (τ < 100 ns) has been attributed to self-quenching between encapsulated RuDCBPY complexes while the slowly decaying population τ > 100 ns has been attributed to RuDCBPY incorporated into the Uio-67 framework. High doping concentrations results in self-quenching by dipole-dipole resonance energy transfer (RET) due to the closer proximity of neighboring RuDCBPY complexes.

Attempts have also been made to grow thin films of RuDCBPY-Uio-67 onto fluorine-doped tin oxide (FTO) and glass sides [39]. The solid state platform allows for numerous applications including electro-chemiluminescence and in chemical and biological sensing [40]. The RuDCBPY-Uio-67 thin film on FTO using a 16.6 mM RuDCBPY loading exhibits an emission decay that best fits to a biexponential decay function with both components displaying a shorter lifetime relative to RuDCBPY-Uio-67. Similar photophysics are observed for higher RuDCBPY concentrations (> 20 mM) with the observed decay lifetimes decreasing as the concentration of RuDCBPY increases. The quenched lifetimes associated with the FTO materials was attributed to a more dense population of RuDCBPY within the Uio-67 framework due to electrostatic interactions between the ruthenium complex and the BPDC/self-assembled monolayer (SAM) that forms onto the FTO slide prior to thin film synthesis. Utilizing the observed emission lifetime (τ_{obs}), the acceptor-

Table 5. Emission lifetime and separation distance of RuDCBPY-Uio-67-DCBPY at various doping concentrations.

Sample	Loading (mM)	τ_{obs} (ns)	r (Å)
RuDCBPY-Uio-67-DCBPY	1	126	22.4
	17	106	21.7
	52	70	20.2
	141	97	21.4

donor distance (r) was calculated using the resonance energy transfer model proposed by Inokuti and Hirayami [41] and found to be ~ 30 Å for Å RuDCBPY-Uio-67 (FTO) at 6.2 mM loading.

Post-synthetic doping of $Ru(Bpy)_2Cl_2$ has also been performed on Uio-67-DCBPY. The attachment of the DCBPY instead of the parent biphenyl dicarboxylate allows for insertion of $Ru(Bpy)_2$ ion and greater control of the loading capacity (RuDCBPY-Uio-67-DCBPY) [42]. The doping concentrations of $Ru(Bpy)_2Cl_2$ were varied between 1 mM to 141 mM while incubated with Uio-67-DCBPY in ethanol. Interestingly, the emission lifetime of RuDCBPY-Uio-67-DCBPY was unaffected by changes in doping concentration (Table 5). Emission lifetimes observed for the low-doped (1 mM) and high-doped (141 mM) RuDCBPY-Uio-67-DCBPY ranged between 70-130 ns when fit to a mono exponential decay function. The single exponential decay indicates a single population of RuDCBPY which is associated with post synthetic incorporation of $Ru(Bpy)_2$ into the framework. Comparison of the lifetimes between solvothermal RuDCBPY-Uio-67 and post synthetic RuDCBPY-Uio-67-DCBPY indicates that the more highly doped RuDCBPY-Uio-67 resembles all doping concentrations of RuDCBPY-Uio-67-DCBPY while the low-doped RuDCBPY-Uio-67 differs considerably exhibiting a long lifetime component (~1.4 μs).

A decrease in the emission lifetime observed for the RuDCBPY-Uio-67-DCBPY with higher loadings was attributed to resonance energy transfer between dense RuDCBPY centers within the framework at high doping concentrations much like RuDCBPY-Uio-67. The spatial emission profile of single crystals of RuDCBPY-Uio-67-DCBPY indicates that at low doping concentrations of $Ru(Bpy)_2Cl_2$, most of the incorporation sites are located on the outermost layers of the crystal relative to the interior. In fact, RuDCBPY concentrates mostly on the vertices and edges of the crystal which indicates two-dimensional fluorescence resonance energy transfer (FRET). Similar FRET processes are observed on surface-absorbed donor-acceptor pairs at saturated RuDCBPY concentrations.

Future perspective

The results summarized here demonstrate the ability to both covalently and non-covalently encapsulate photoactive Ru(II) polyimine complexes within highly robust Zr-O porous MOF materials. The encapsulation results in modulation of the metal complex photophysics with the lifetime extension of the ^{3}MLCT state being the most advantageous for light harvesting applications. Longer lifetimes lead to significantly increased quantum yields for photochemical processes. The successful encapsulation of Ru(II) polyimine complexes also suggests other transition metal complexes can be readily encapsulated within Zr-O MOFs including Ir, Rh, Re and Cr ligand complexes. For example, encapsulation of either $Re(I)(bpy)(CO)_3L$ (L=$P(Et)_3$, NCS; bpy = 2,2'-bipyridine) or Ir(III) terpyridine complexes can lead to new heterogeneous photocatalysts for CO_2 reduction while expanded libraries of Ru(II) complexes containing hemolytic or heterolytic polyimines will be useful for energy transfer materials. Mixed bed MOFs containing mixed metal polyimines encapsulated within Zr-O MOFs may also lead to directional photoinduced electron transfer which is critically important for photovoltaic applications. Finally, the ability to form thin films of Zr-O MOFs containing encapsulated photoactive transition metal complexes opens new avenues for robust MOF-based device fabrication for light harvesting applications.

CONFLICT OF INTEREST STATEMENT

There are no conflicts of interest.

REFERENCES

1. Aiken III, J. D. F. and Richard G. 1999, Journal of Molecular Catalysis A: Chemical, 145, 1-44.
2. Matsuda, Y., Shin, D. N. and Bernstein, E. R. 2004, J. Chem. Phys., 120(9), 4142-4149.
3. Kato, S., Otake, K. I., Chen, H., Akpinar, I., Buru, C. T., Islamoglu, T., Snurr, R. Q. and Farha, O. K. 2019, J. Am. Chem. Soc., 141(6), 2568-2576.
4. Lee, C. Y., Farha, O. K., Hong, B. J., Sarjeant, A. A., Nguyen, S. T. and Hupp, J. T. 2011, J. Am. Chem. Soc., 133(40), 15858.
5. Eddaoudi, M., Sava, D. F., Eubank, J. F., Adil, K. and Guillerm, V. 2015, Chem. Soc. Rev., 44(1), 228-249.
6. Zhou, H. C., Long, J. R. and Yaghi, O. M. 2012, Chem. Rev., 112(2), 673-674.
7. Perry, J. J., Perman, J. A. and Zaworotko, M. J. 2009, Chem. Soc. Rev., 38(5), 1400-1417.
8. Plonka, A. M., Wang, Q., Gordon, W. O., Balboa, A., Troya, D., Guo, W., Sharp, C. H., Senanayake, S. D., Morris, J. R., Hill, C. L. and Frenkel, A. I. 2017, J. Am. Chem. Soc., 139(2), 599-602.
9. Islamoglu, T., Otake, K.-i., Li, P., Buru, C. T., Peters, A. W., Akpinar, I., Garibay, S. J. and Farha, O. K. 2018, CrystEngComm, 20(39), 5913-5918.
10. Qin, J., Yuan, S., Zhang, L., Li, B., Du, D. Y., Huang, N., Guan, W., Drake, H., Pang, J., Lan, Y. Q., Alsalme, A. and Zhou, H. C. 2019, J. Am. Chem. Soc., 141(5), 2054-2060.
11. Burtch, N. C., Jasuja, H. and Walton, K. S. 2014, Chem. Rev., 114(20), 10575-10612.
12. Bai, Y., Dou, Y., Xie, L. H., Rutledge, W., Li, J. R. and Zhou, H. C. 2016, Chem. Soc. Rev., 45(8), 2327-67.
13. Cavka, J. H., Jakobsen, S., Olsbye, U., Guillou, N., Lamberti, C., Bordiga, S. and Lillerud, K. P. 2008, J. Am. Chem. Soc., 130, 13850-13851.
14. Morris, W., Volosskiy, B., Demir, S., Gandara, F., McGrier, P. L., Furukawa, H., Cascio, D., Stoddart, J. F. and Yaghi, O. M. 2012, Inorg. Chem., 51(12), 6443-6445.
15. Jiang, J., Gandara, F., Zhang, Y. B., Na, K., Yaghi, O. M. and Klemperer, W. G. 2014, J. Am. Chem. Soc., 136(37), 12844-12847.
16. Furukawa, H., Gandara, F., Zhang, Y. B., Jiang, J., Queen, W. L., Hudson, M. R. and Yaghi, O. M. 2014, J. Am. Chem. Soc., 136(11), 4369-4381.
17. Meyer, T. J. 1986, Pure Appl. Chem., 58(9), 1193-1206.
18. Larsen, R. W. and Wojtas, L. 2017, J. Solid State Chem., 247, 77-82.
19. Mayers, J. M. and Larsen, R. W. 2019, Polyhedron, 171, 382-388.
20. Larsen, R. W. and Wojtas, L. 2012, J. Phys. Chem. A., 116(30), 7830-7835.
21. Larsen, R. W. and Wojtas, L. 2017, Inorganica Chimica Acta, 466, 243-248.
22. McKeithan, C. R., Mayers, J. M., Wojtas, L. and Larsen, R. W. 2018, Inorganica Chimica Acta, 483, 1-5.
23. Whittington, C. L., Wojtas, L. and Larsen, R. W. 2014, Inorg. Chem., 53(1), 160-166.
24. Whittington, C. L., Wojtas, L., Gao, W. Y., Ma, S. and Larsen, R. W. 2015, Dalton Trans., 44(12), 5331-5337.
25. Larsen, R. W., Mayers, J. M. and Wojtas, L. 2017, Dalton Trans., 46(37), 12711-12716.
26. McKeithan, C. F. W., Lukasz Larsen and Randy, W. 2019, Inorganica Chimica Acta., 496, 119034.
27. Caspar, J. V. and Meyer, T. J. 1983, Inorg. Chem., 22(17), 2444-2453.
28. Lainé, P., Lanz, M. and Calzaferri, G. 1996, Inorg. Chem., 35(12), 3514-3518.
29. Incavo, J. A. and Dutta, P. K. 1990, J. Phys. Chem., 94, 3075-3081.
30. Karki, L. and Hupp, J. T. 1997, Inorg. Chem., 36, 3318-3321.
31. Hug, S. J. and Boxer, S. G. 1996, Inorganica Chimica Acta, 242(1), 323-327.
32. Maruszewski, K., Strommen, D. P. and Kincaid, J. R. 1993, J. Am. Chem. Soc., 115(18), 8345-8350.
33. Lumpkin, R. S., Kober, E. M., Worl, L. A., Murtaza, Z. and Meyer, T. J. 1990, J. Phys. Chem., 94(1), 239-243.
34. Matsui, K. M. and Fumitoshi. 1997, Chem. Mater., 9, 2588-2591.
35. Marti, A. A. and Colon, J. L. 2010, Inorg. Chem., 49(16), 7298-7303.

36. Wasielewski, M. R. 1992, Chem. Rev., 92, 435-461.
37. Mohan, N., Vijayalakshmi, K. P., Koga, N. and Suresh, C. H. 2010, J. Comput. Chem., 31(16), 2874-2882.
38. Maza, W. A. and Morris, A. J. 2014, J. Phys. Chem. C., 118(17), 8803-8817.
39. Maza, W. A., Ahrenholtz, S. R., Epley, C. C., Day, C. S. and Morris, A. J. 2014, J. Phys. Chem. C., 118(26), 14200-14210.
40. Cai, M., Loague, Q. R., Zhu, J., Lin, S., Usov, P. M. and Morris, A. J. 2018, Dalton Trans., 47(46), 16807-16812.
41. Inokuti, M. and Hirayama, F. 1965, J. Chem. Phys., 43(6), 1978-1989.
42. Maza, W. A., Padilla, R. and Morris, A. J. 2015, J. Am. Chem. Soc., 137(25), 8161-8168.